Extended lattice Boltzmann model for gas dynamics EP

M. H. Saadat, S. A. Hosseini, B. Dorschner, et al.

COLLECTIONS

EP This paper was selected as an Editor's Pick

View Online   Export Citation   CrossMark

ARTICLES YOU MAY BE INTERESTED IN

On the lattice Boltzmann method and its application to turbulent, multiphase flows of various fluids including cryogens: A review
Physics of Fluids **33**, 041302 (2021); https://doi.org/10.1063/5.0046938

Simulation of flow induced by single-dielectric-barrier-discharge plasma actuator using a high-order flux-reconstruction scheme
Physics of Fluids **33**, 047108 (2021); https://doi.org/10.1063/5.0046900

A three-dimensional phase-field lattice Boltzmann method for incompressible two-components flows
Physics of Fluids **33**, 043315 (2021); https://doi.org/10.1063/5.0046875

Extended lattice Boltzmann model for gas dynamics (EP)

View Online   Export Citation   CrossMark

M. H. Saadat, (iD) S. A. Hosseini, (iD) B. Dorschner, (iD) and I. V. Karlin[a] (iD)

AFFILIATIONS

Department of Mechanical and Process Engineering, ETH Zurich, 8092 Zurich, Switzerland

[a]Author to whom correspondence should be addressed: ikarlin@ethz.ch

ABSTRACT

We propose a two-population lattice Boltzmann model on standard lattices for the simulation of compressible flows. The model is fully on-lattice and uses the single relaxation time Bhatnagar–Gross–Krook kinetic equations along with appropriate correction terms to recover the Navier–Stokes–Fourier equations. The accuracy and performance of the model are analyzed through simulations of compressible benchmark cases including Sod shock tube, sound generation in shock–vortex interaction, and compressible decaying turbulence in a box with eddy shocklets. It is demonstrated that the present model provides an accurate representation of compressible flows, even in the presence of turbulence and shock waves.

I. INTRODUCTION

The development of accurate and efficient numerical methods for the simulation of compressible fluid flows remains a highly active research field in computational fluid dynamics (CFD), and is of great importance to many natural phenomena and engineering applications. Compressibility is usually measured by the Mach number, $Ma = u/c_s$, defined as the ratio of the flow velocity to the speed of sound and is mainly characterized by the importance of density and temperature variations and a dilatational velocity component. The presence of shock waves in compressible flows also poses severe challenges for an accurate numerical simulation. Shock waves are sharp discontinuities of the flow properties across a thin region with the thickness of the order of mean free path. Since in practical simulations, it is impossible to use a grid size fine enough to resolve the physical shock structure defined by the molecular viscosity, most numerical schemes rely on some numerical dissipation to stabilize the simulation and capture the shock over a few grid points.[1,2] The additional numerical dissipation of shock-capturing schemes, however, is problematic in smooth turbulent regions of the flow, where a nondissipative scheme is required to capture the complex physics accurately. Therefore, in recent years, much effort has been devoted to developing numerical schemes capable of treating shocks and turbulence, simultaneously. This has resulted in various improvements of the weighted essentially non-oscillatory (WENO) scheme,[3–6] artificial diffusivity approaches,[7] and hybrid schemes,[8] to name a few.

In the past decades, the lattice Boltzmann method (LBM) has received considerable attention for CFD as a kinetic theory approach based on the discrete Boltzmann equation. LBM has been proved to be a viable and efficient tool for the simulation of complex fluid flows and has been applied to a wide range of fluid dynamics problems including, but not limited to, turbulence,[9] multi-phase flows,[10] and relativistic hydrodynamics.[11] The attractiveness of the LBM over conventional CFD methods lies in the simplicity and locality of its underlying numerical algorithm which can be summarized as "stream populations along the discrete velocities c_i and equilibrate at the nodes x." It is, however, well known that LBM faces stiff challenges in dealing with high-speed flows and its success has been mainly limited to low-speed incompressible flow applications.

While LBM on standard lattices recovers the Navier–Stokes (NS) equations in the hydrodynamic limit, there exist Galilean noninvariant error terms in the stress tensor which are negligible only in the limit of vanishing velocities and at a singular temperature, known as the lattice temperature. This prevents LBM from going to higher velocities as well as incorporating temperature dynamics. A natural approach to overcome this limitation is to include more discrete velocities and use the hierarchy of admissible high-order (or multi-speed) lattices[12,13] to ensure the Galilean invariance and temperature independence of the stress tensor. Although models based on high-order lattices[14,15] have been shown to be successful in simulating compressible flows to some

extent, they increase significantly the computational cost and suffer from a limited temperature range,[16] as well.

Another approach, which has received considerable attention in recent years, maintains the simplicity and efficiency of the standard lattices and employs correction terms in order to remove the aforementioned spurious terms in the stress tensor.[17,18] Due to intrinsic nonuniqueness of the correction term, different implementations exist in the literature, all recover the same equations in the hydrodynamic limit.[19–21] See Hosseini et al.[22] for a detailed review of different implementations. Besides correction term, to fully recover the Navier–Stokes–Fourier (NSF) equations, one also needs to incorporate the energy equation. For doing that different models have been proposed in the literature which, in general, can be categorized into two main groups: hybrid and two-population methods. Hybrid methods[23–26] rely on solving the total energy/entropy equation using conventional numerical schemes like finite-difference or finite-volume. Furthermore, multi-relaxation time collision operators, such as the hybrid regularized recursive model, are required to achieve high subsonic and supersonic regimes.[26] The majority of hybrid LB schemes also suffer from lack of energy conservation, as the energy equation is solved in a nonconservative form,[27] and resolving this issue is still an ongoing research.[27–29] In the two-population approach,[19,21,30,31] however, another population is used for the conservation of total energy. The latter provides a fully conservative and unified kinetic framework for the compressible flows. Earlier models[19,30,31] within the two-population framework on standard lattices were limited to low-Mach thermal applications. Recent models[21,32] have successfully tackled high-speed compressible flows. However, in those models the simulation of supersonic flows was based on the concept of shifted lattices[33] or adaptive lattices[34] and needed some form of interpolation during the streaming step. Therefore, a fully on-lattice conservative scheme capable of capturing the complex physics of compressible flows involving shock waves is still needed.

In this paper, we revisit and propose a two-population realization of the compressible LB model on standard lattices through two key modifications compared to previous models:[21,32] (1) use of the product-form formulation of equilibrium for the total energy population which recovers all Maxwell–Boltzmann (MB) moments supported by the stencil, and (2) new correction terms to consistently restore the stress tensor and viscous heat dissipation. Furthermore, upwind-discretization is used for correction terms to enhance the stability of high Mach flows. The resulting model is a fully on-lattice model which uses the single relaxation time (SRT) Bhatnagar–Gross–Krook[35] collision term and is capable of capturing moderately supersonic regimes including shock waves. Through the Chapman–Enskog analysis, the model is shown to recover the compressible NSF equations with adjustable Prandtl number and adiabatic exponent in the hydrodynamic limit. We then investigate the accuracy and performance of the model for a range of compressible cases from subsonic to the moderately supersonic regime with shock waves and turbulence. It is shown that computing the correction terms with the upwind scheme provides enough numerical dissipation to avoid the Gibbs oscillations, and to effectively capture the shock waves without degrading the accuracy of the scheme and overwhelming the physical dissipation in smooth regions. This is demonstrated through the simulation of acoustic waves in the shock–vortex interaction problem. We then investigate a more challenging case of compressible decaying isotropic turbulence at large turbulent Mach and Reynolds numbers, where the interaction of compressibility effects, turbulence, and shocks are present in the flow field.

The remainder of the paper is organized as follows: the kinetic equations of the two-population compressible LB model along with the pertinent equilibrium and quasi-equilibrium populations are presented in Sec. II. In Sec. III, the model is validated and analyzed through simulation of benchmark test-cases, including Sod shock-tube, shock–vortex interaction, and decaying of a compressible isotropic turbulence. Conclusions are drawn in Sec. IV.

II. MODEL DESCRIPTION

A. Kinetic equations

In the two-population approach, conservation laws are split between the two sets. A set of f-populations f_i represents mass and momentum while another set of g-populations g_i is earmarked for the energy conservation. Following Karlin et al.,[31] we consider a single relaxation time lattice Bhatnagar–Gross–Krook (LBGK) equations for the f-populations and a quasi-equilibrium LBM equation for the g-populations, corresponding to discrete velocities c_i, where $i = 0, \ldots, Q-1$,

$$f_i(\boldsymbol{x} + \boldsymbol{c}_i \delta t, t + \delta t) - f_i(\boldsymbol{x}, t) = \omega(f_i^{\text{ex}} - f_i), \quad (1)$$

$$g_i(\boldsymbol{x} + \boldsymbol{c}_i \delta t, t + \delta t) - g_i(\boldsymbol{x}, t) = \omega_1(g_i^{\text{eq}} - g_i) + (\omega - \omega_1)(g_i^{\text{eq}} - g_i^*). \quad (2)$$

The extended equilibrium f_i^{ex}, the equilibrium g_i^{eq} and the quasi-equilibrium g_i^* satisfy the local conservation laws for the density ρ, momentum $\rho\boldsymbol{u}$ and energy ρE,

$$\rho = \sum_{i=0}^{Q-1} f_i^{\text{ex}} = \sum_{i=0}^{Q-1} f_i, \quad (3)$$

$$\rho\boldsymbol{u} = \sum_{i=0}^{Q-1} \boldsymbol{c}_i f_i^{\text{ex}} = \sum_{i=0}^{Q-1} \boldsymbol{c}_i f_i, \quad (4)$$

$$\rho E = \sum_{i=0}^{Q-1} g_i^{\text{eq}} = \sum_{i=0}^{Q-1} g_i^* = \sum_{i=0}^{Q-1} g_i. \quad (5)$$

We consider a general caloric equation of state of ideal gas. Without loss of generality, the reference temperature is set at $T = 0$ and the internal energy at unit density U is written as

$$U = \int_0^T C_v(T) dT, \quad (6)$$

where T is the temperature and $C_v(T)$ is the mass-based specific heat at constant volume. The energy at unit density E is

$$E = U + \frac{u^2}{2}. \quad (7)$$

The relaxation parameters ω and ω_1 are related to viscosity and thermal conductivity, as it will be shown below. We now proceed with specifying the equilibria and quasi-equilibria for the standard lattice.

B. Discrete velocities and factorization

We consider the $D3Q27$ set of three-dimensional discrete velocities c_i, where $D = 3$ is the space dimension and $Q = 27$ is the number of discrete speeds,

$$c_i = (c_{ix}, c_{iy}, c_{iz}), \quad c_{i\alpha} \in \{-1, 0, 1\}, \quad i = 0, \dots, 26. \tag{8}$$

Below, we make use of a product-form to represent all pertinent populations, the extended f-equilibrium, and the g-equilibrium and g-quasi-equilibrium, featured in the relaxation terms of (1) and (2). We follow Karlin and Asinari[36] and consider a triplet of functions in two variables ξ and $\mathcal{P}$,

$$\Psi_0(\xi, \mathcal{P}) = 1 - \mathcal{P}, \tag{9}$$

$$\Psi_1(\xi, \mathcal{P}) = \frac{1}{2}(\xi + \mathcal{P}), \tag{10}$$

$$\Psi_{-1}(\xi, \mathcal{P}) = \frac{1}{2}(-\xi + \mathcal{P}). \tag{11}$$

For vector-parameters (ξ_x, ξ_y, ξ_z) and $(\mathcal{P}_{xx}, \mathcal{P}_{yy}, \mathcal{P}_{zz})$, we consider a product associated with the speeds c_i (8),

$$\Psi_i = \Psi_{c_{ix}}(\xi_x, \mathcal{P}_{xx})\Psi_{c_{iy}}(\xi_y, \mathcal{P}_{yy})\Psi_{c_{iz}}(\xi_z, \mathcal{P}_{zz}). \tag{12}$$

The moments of the product-form (12),

$$\mathcal{M}_{lmn} = \sum_{i=0}^{26} c_{ix}^l c_{iy}^m c_{iz}^n \Psi_i, \tag{13}$$

are readily computed thanks to the factorization,

$$\mathcal{M}_{lmn} = \mathcal{M}_{l00}\mathcal{M}_{0m0}\mathcal{M}_{00n}, \tag{14}$$

where $\mathcal{M}_{000} = 1$, and

$$\mathcal{M}_{l00} = \begin{cases} \xi_x, & l \text{ odd} \\ \mathcal{P}_{xx}, & l \text{ even}, \end{cases} \tag{15}$$

$$\mathcal{M}_{0m0} = \begin{cases} \xi_y & m \text{ odd} \\ \mathcal{P}_{yy} & m \text{ even}, \end{cases} \tag{16}$$

$$\mathcal{M}_{00n} = \begin{cases} \xi_z & n \text{ odd} \\ \mathcal{P}_{zz} & n \text{ even}. \end{cases} \tag{17}$$

With the product-form (12), we proceed to specifying the extended equilibrium f-populations f_i^{ex} in (1), and the equilibrium g-populations g_i^{eq} and the quasi-equilibrium g-populations g_i^* in (2).

C. Extended f-equilibrium

The extended equilibrium featured in the LBGK equation (1) has been already introduced by Saadat et al.[37] for the fixed temperature case. We shall summarize the construction for the purpose of the present compressible flow situation. At first, we define the equilibrium f_i^{eq} by specifying,

$$\xi_\alpha = u_\alpha, \tag{18}$$

$$\mathcal{P}_{\alpha\alpha}^{\text{eq}} = RT + u_\alpha^2. \tag{19}$$

Substituting (18) and (19) into (12), we obtain,

$$f_i^{\text{eq}} = \rho\Psi_{c_{ix}}(u_x, \mathcal{P}_{xx}^{\text{eq}})\Psi_{c_{iy}}(u_y, \mathcal{P}_{yy}^{\text{eq}})\Psi_{c_{iz}}(u_z, \mathcal{P}_{zz}^{\text{eq}}). \tag{20}$$

The factorization (14) implies that equilibrium (20) verifies the maximal number $Q = 27$ of the moment relations established by the Maxwell–Boltzmann (MB) distribution,

$$\sum_{i=0}^{26} c_{ix}^l c_{iy}^m c_{iz}^n f_i^{\text{eq}} = F_{lmn}^{\text{MB}}, \quad l, m, n \in \{0, 1, 2\}, \tag{21}$$

where

$$F_{lmn}^{\text{MB}} = \rho(2\pi RT)^{-\frac{3}{2}} \int c_x^l c_y^m c_z^n e^{-\frac{(c-u)^2}{2RT}} d\mathbf{c}. \tag{22}$$

Furthermore, with (14), we find the pressure tensor and the third-order moment tensor at the equilibrium (20),

$$\mathbf{P}^{\text{eq}} = \sum_{i=0}^{26} \mathbf{c}_i \otimes \mathbf{c}_i f_i^{\text{eq}} = \mathbf{P}^{\text{MB}}, \tag{23}$$

$$\mathbf{Q}^{\text{eq}} = \sum_{i=0}^{26} \mathbf{c}_i \otimes \mathbf{c}_i \otimes \mathbf{c}_i f_i^{\text{eq}} = \mathbf{Q}^{\text{MB}} + \tilde{\mathbf{Q}}. \tag{24}$$

Here, the isotropic parts, $\mathbf{P}^{\text{MB}}$ and $\mathbf{Q}^{\text{MB}}$, are the Maxwell–Boltzmann pressure tensor and the third-order moment tensor, respectively,

$$\mathbf{P}^{\text{MB}} = P\mathbf{I} + \rho\mathbf{u} \otimes \mathbf{u}, \tag{25}$$

$$\mathbf{Q}^{\text{MB}} = \text{sym}(P\mathbf{I} \otimes \mathbf{u}) + \rho\mathbf{u} \otimes \mathbf{u} \otimes \mathbf{u}, \tag{26}$$

where $P = \rho RT$ is the pressure, $\text{sym}(\cdots)$ denotes symmetrization and $\mathbf{I}$ is the unit tensor.

The anisotropy of the equilibrium (20) manifests with the deviation $\tilde{\mathbf{Q}} = \mathbf{Q}^{\text{eq}} - \mathbf{Q}^{\text{MB}}$ in (24), where only the diagonal elements are nonvanishing,

$$\tilde{Q}_{\alpha\beta\gamma} = \begin{cases} \rho u_\alpha(1 - 3RT) - \rho u_\alpha^3 & \text{if } \alpha = \beta = \gamma \\ 0 & \text{otherwise}. \end{cases} \tag{27}$$

The origin of the diagonal anomaly (27) is the geometric constraint featured by the discrete speeds (8), $c_{i\alpha}^3 = c_{i\alpha}$, for any $i = 0, \dots, 26$. Put differently, the equilibrium pressure tensor (23) and the off diagonal elements of the equilibrium third-order moments (24) are included in the set of independent moments (21), hence they verify the Maxwell–Boltzmann moment relations by the product-form. Contrary to that, the diagonal components $Q_{\alpha\alpha\alpha}^{\text{eq}}$ are not among the set of moments (8), hence the anomaly. A remedy, commonly employed in the conventional LBM for incompressible flow simulations, is to minimize the spurious effects of the said anisotropy by fixing the lattice reference temperature, $RT_L = 1/3$ in order to eliminate the linear term $O(u_\alpha)$ in (27). Thus, the use of the equilibrium (20) in the LBGK equation (1) imposes a twofold restriction: the temperature cannot be chosen differently from T_L while at the same time the flow velocity has to be maintained asymptotically vanishing. While the equilibrium (20) can still be used for the thermal LBM in the Bussinesq approximation,[31] they make (20) insufficient for a compressible flow setting.

Instead, as was proposed by Saadat et al.,[37] the equilibrium (20) needs to be extended in such a way that the third-order moment anomaly (27) is compensated in the hydrodynamic limit. Because the anomaly only concerns the diagonal elements of the third-order moments, the cancelation is achieved by redefining the diagonal elements of the second-order moments $\mathcal{P}_{\alpha\alpha}$. As was demonstrated in Ref. 37, in order the achieve cancelation of the errors, the diagonal elements $\mathcal{P}_{\alpha\alpha}^{\text{ex}}$ must be extended as

$$\mathcal{P}_{\alpha\alpha}^{\text{ex}} = \mathcal{P}_{\alpha\alpha}^{\text{eq}} + \delta t\left(\frac{2 - \omega}{2\rho\omega}\right)\partial_\alpha\tilde{Q}_{\alpha\alpha\alpha}, \tag{28}$$

where $\partial_\alpha = \partial/\partial x_\alpha$ and $\tilde{Q}_{\alpha\alpha\alpha}$ is the diagonal element of the anomaly (27),

$$\tilde{Q}_{\alpha\alpha\alpha} = \rho u_\alpha(1 - 3RT) - \rho u_\alpha^3. \qquad (29)$$

With (28) instead of (19), the extended equilibrium f_i^{ex} is defined using the product form as before,

$$f_i^{ex} = \rho\Psi_{c_{ix}}(u_x, \mathcal{P}_{xx}^{ex})\Psi_{c_{iy}}(u_y, \mathcal{P}_{yy}^{ex})\Psi_{c_{iz}}(u_z, \mathcal{P}_{zz}^{ex}). \qquad (30)$$

The pressure tensor of the extended equilibrium is thus

$$\boldsymbol{P}^{ex} = \boldsymbol{P}^{eq} + \delta t\left(\frac{2 - \omega}{2\omega}\right)\boldsymbol{\nabla}\cdot\tilde{\boldsymbol{Q}}. \qquad (31)$$

As it has been shown in Ref. 37, when the extended equilibrium (30) is used in the LBGK equation (1) at a fixed temperature T, the Navier–Stokes equation for the flow momentum is recovered in a range of flow velocities and temperatures. However, in the problem under consideration, the temperature is input from the g-population dynamics, specifically, by solving the integral equation (7). We thus turn our attention to specifying the equilibrium and the quasi-equilibrium in the g-kinetic equation (2).

D. g-Equilibrium and g-quasi-equilibrium

We first consider the moments of the Maxwell–Boltzmann energy distribution function,

$$G_{lmn}^{MB} = \rho(2\pi RT)^{-\frac{3}{2}}\int c_x^l c_y^m c_z^n\left(\frac{c^2}{2}e^{-\frac{(c-u)^2}{2RT}}\right)d\boldsymbol{c}. \qquad (32)$$

Let us introduce operators $\mathcal{O}_\alpha$ acting on any smooth function $A(\boldsymbol{u}, T)$ as follows:[31]

$$\mathcal{O}_\alpha A = RT\frac{\partial A}{\partial u_\alpha} + u_\alpha A. \qquad (33)$$

The Maxwell–Boltzmann energy moments (32) can be written as the result of repeated application of operators (33) on the generating function,

$$G_{lmn}^{MB} = \rho\mathcal{O}_x^l\mathcal{O}_y^m\mathcal{O}_z^n E^{MB}, \qquad (34)$$

where the generating function E^{MB} is the energy of the ideal monatomic gas at unit density (three translational degrees of freedom, $C_v = (3/2)R$),

$$E^{MB} = \frac{3}{2}RT + \frac{u^2}{2}. \qquad (35)$$

Next, we extend the Maxwell–Boltzmann energy moments (34) to a general caloric ideal gas equation of state (7). This amounts to replacing the generating function (35) with the energy (7),

$$G_{lmn}^{eq} = \rho\mathcal{O}_x^l\mathcal{O}_y^m\mathcal{O}_z^n E. \qquad (36)$$

Among the higher-order moments (36), we recognize those pertinent to the hydrodynamic limit of the energy equation to be analyzed below. These are the equilibrium energy flux $\boldsymbol{q}^{eq}$ and the flux of the energy flux tensor $\boldsymbol{R}^{eq}$,

$$q_\alpha^{eq} = \rho\mathcal{O}_\alpha E = \left(H + \frac{u^2}{2}\right)\rho u_\alpha, \qquad (37)$$

$$R_{\alpha\beta}^{eq} = \rho\mathcal{O}_\alpha\mathcal{O}_\beta E = \left(H + \frac{u^2}{2}\right)P_{\alpha\beta}^{eq} + Pu_\alpha u_\beta. \qquad (38)$$

Here H is the specific enthalpy,

$$H = \int_0^T C_p(T)dT, \qquad (39)$$

while C_p is the specific heat at constant pressure, satisfying Mayer's relation, $C_p - C_v = R$.

The equilibrium populations g_i^{eq} are specified with the operator version of the product-form (12). To that end, we consider parameters ξ_α and $\mathcal{P}_{\alpha\alpha}$ as operator symbols,

$$\xi_\alpha = \mathcal{O}_\alpha, \qquad (40)$$

$$\mathcal{P}_{\alpha\alpha} = \mathcal{O}_\alpha^2. \qquad (41)$$

With the operators (40) and (41) substituted into the product form (12), the equilibrium populations g_i^{eq} are written using the generating function (7),

$$g_i^{eq} = \rho\Psi_{c_{ix}}(\mathcal{O}_x, \mathcal{O}_x^2)\Psi_{c_{iy}}(\mathcal{O}_y, \mathcal{O}_y^2)\Psi_{c_{iz}}(\mathcal{O}_z, \mathcal{O}_z^2)E. \qquad (42)$$

With (14), it is straightforward to see that the equilibrium (42) verifies a subset of the equilibrium energy moments (36),

$$\sum_{i=0}^{26}c_{ix}^l c_{iy}^m c_{iz}^n g_i^{eq} = G_{lmn}^{eq}, \quad l, m, n \in \{0, 1, 2\}. \qquad (43)$$

Thus, by construction, the g-equilibrium (42) recovers the maximal number $Q = 27$ of the energy moments (36), including the energy flux (37) and the flux of the energy flux (38).

Finally, similarly to,[31] the quasi-equilibrium populations g_i^* are needed for adjusting the Prandtl number of the model. To that end, the quasi-equilibrium g_i^* differs from g_i^{eq} by the nonequilibrium energy flux only,

$$g_i^* = \begin{cases} g_i^{eq} + \dfrac{1}{2}\boldsymbol{c}_i\cdot(\boldsymbol{q}^* - \boldsymbol{q}^{eq}) & \text{if } c_i^2 = 1 \\ g_i^{eq} & \text{otherwise.} \end{cases} \qquad (44)$$

Here $\boldsymbol{q}^*$ is a specified quasi-equilibrium energy flux. Indeed, (44) and (43) imply for $l, m, n \in \{0, 1, 2\}$,

$$\sum_{i=0}^{26}c_{ix}^l c_{iy}^m c_{iz}^n g_i^* = \begin{cases} q_x^* & \text{if } l = 1, m = 0, n = 0 \\ q_y^* & \text{if } l = 0, m = 1, n = 0 \\ q_z^* & \text{if } l = 0, m = 0, n = 1 \\ G_{lmn}^{eq} & \text{otherwise.} \end{cases} \qquad (45)$$

While the above construction holds for any specified $\boldsymbol{q}^*$, the quasi-equilibrium flux required for the consistent realization of the adjustable Prandtl number by the LBM system (1) and (2) reads,

$$\boldsymbol{q}^* = \boldsymbol{q}^{eq} + \boldsymbol{u}\cdot\left(\boldsymbol{P} - \boldsymbol{P}^{eq} + \frac{\delta t}{2}\boldsymbol{\nabla}\cdot\tilde{\boldsymbol{Q}}\right), \qquad (46)$$

where $\boldsymbol{P}$ is the pressure tensor,

$$P = \sum_{i=0}^{26} c_i \otimes c_i f_i. \tag{47}$$

Note that unlike in the original incompressible thermal model,[31] the quasi-equilibrium flux (46) now includes an extension due to the diagonal anomaly. With all the elements of the LBM system (1) and (2) specified, we now proceed with working out its hydrodynamic limit.

E. Hydrodynamic limit

Taylor expansion of the shift operator in (1) and (2) to second-order gives

$$\left[\delta t D_i + \frac{\delta t^2}{2} D_i D_i \right] f_i = \omega(f_i^{\mathrm{ex}} - f_i), \tag{48}$$

$$\left[\delta t D_i + \frac{\delta t^2}{2} D_i D_i \right] g_i = \omega_1(g_i^{\mathrm{eq}} - g_i) + (\omega - \omega_1)(g_i^{\mathrm{eq}} - g_i^*), \tag{49}$$

where D_i is the derivative along the characteristics,

$$D_i = \partial_t + c_i \cdot \nabla. \tag{50}$$

Introducing a multi-scale expansion,

$$f_i = f_i^{(0)} + \delta t f_i^{(1)} + \delta t^2 f_i^{(2)} + O(\delta t^3), \tag{51}$$

$$f_i^{\mathrm{ex}} = f_i^{\mathrm{ex}(0)} + \delta t f_i^{\mathrm{ex}(1)} + \delta t^2 f_i^{\mathrm{ex}(2)} + O(\delta t^3), \tag{52}$$

$$g_i = f_i^{(0)} + \delta t f_i^{(1)} + \delta t^2 f_i^{(2)} + O(\delta t^3), \tag{53}$$

$$g_i^* = g_i^{*(0)} + \delta t g_i^{*(1)} + \delta t^2 g_i^{*(2)} + O(\delta t^3), \tag{54}$$

$$\partial_t = \partial_t^{(1)} + \delta t \partial_t^{(2)} + O(\delta t^2), \tag{55}$$

substituting into (48) and (49), and using the notation,

$$D_i^{(1)} = \partial_t^{(1)} + c_i \cdot \nabla, \tag{56}$$

we obtain, from zeroth through second order in the time step δt, for the f-populations,

$$f_i^{(0)} = f_i^{\mathrm{ex}(0)} = f_i^{\mathrm{eq}}, \tag{57}$$

$$D_i^{(1)} f_i^{(0)} = -\omega\left(f_i^{(1)} - f_i^{\mathrm{ex}(1)}\right), \tag{58}$$

$$\partial_t^{(2)} f_i^{(0)} + c_i \cdot \nabla f_i^{(1)} - \frac{\omega}{2} D_i^{(1)}\left(f_i^{(1)} - f_i^{\mathrm{ex}(1)}\right) = -\omega f_i^{(2)} + \omega f_i^{\mathrm{ex}(2)}, \tag{59}$$

and similarly for the g-populations,

$$g_i^{(0)} = g_i^{*(0)} = g_i^{\mathrm{eq}}, \tag{60}$$

$$D_i^{(1)} g_i^{(0)} = -\omega_1 g_i^{(1)} - (\omega - \omega_1) g_i^{*(1)}, \tag{61}$$

$$\partial_t^{(2)} g_i^{(0)} + c_i \cdot \nabla g_i^{(1)} - \frac{\omega_1}{2} D_i^{(1)} g_i^{(1)} - \frac{\omega - \omega_1}{2} D_i^{(1)} g_i^{*(1)}$$
$$= -\omega_1 g_i^{(2)} - (\omega - \omega_1) g_i^{*(2)}. \tag{62}$$

With (57) and (60), the mass, momentum, and energy conservation (3), (4), and (5) imply the solvability conditions,

$$\sum_{i=0}^{26} f_i^{\mathrm{ex}(k)} = \sum_{i=0}^{26} f_i^{(k)} = 0, \quad k = 1, 2, \dots, \tag{63}$$

$$\sum_{i=0}^{26} c_i f_i^{\mathrm{ex}(k)} = \sum_{i=0}^{26} c_i f_i^{(k)} = 0, \quad k = 1, 2, \dots, \tag{64}$$

$$\sum_{i=0}^{26} g_i^{*(k)} = \sum_{i=0}^{26} g_i^{(k)} = 0, \quad k = 1, 2, \dots. \tag{65}$$

With the f-equilibrium (20) and the g-equilibrium (42), while taking into account the solvability conditions (63), (64), and (65), and also making use of the equilibrium pressure tensor (23) and (25), and the equilibrium energy flux (37), the first-order kinetic equations (58) and (61) imply the following first-order balance equations for the density, momentum, and energy,

$$\partial_t^{(1)} \rho = -\nabla \cdot (\rho u), \tag{66}$$

$$\partial_t^{(1)}(\rho u) = -\nabla \cdot (PI + \rho u \otimes u), \tag{67}$$

$$\partial_t^{(1)}(\rho E) = -\nabla \cdot q^{\mathrm{eq}}. \tag{68}$$

The first-order energy equation (68) can be recast into the temperature equation by virtue of (66) and (67),

$$\rho C_v \partial_t^{(1)} T = -\rho C_v u \cdot \nabla T - P(\nabla \cdot u). \tag{69}$$

Thus, to first order, the LBM recovers the compressible Euler equations for a generic ideal gas.

Moreover, the first-order constitutive relation for the nonequilibrium pressure tensor $P^{(1)}$ is found from (58) as follows, using (25), (24), (26), and (27),

$$-\omega P^{(1)} + \omega P^{\mathrm{ex}(1)} = \partial_t^{(1)} P^{\mathrm{MB}} + \nabla \cdot Q^{\mathrm{MB}} + \nabla \cdot \tilde{Q}, \tag{70}$$

where

$$P^{(1)} = \sum_{i=0}^{Q-1} c_i \otimes c_i f_i^{(1)}, \tag{71}$$

$$P^{\mathrm{ex}(1)} = \sum_{i=0}^{Q-1} c_i \otimes c_i f_i^{\mathrm{ex}(1)}. \tag{72}$$

Using (66), (67), and (69), we find in (70),

$$\partial_t^{(1)} P^{\mathrm{MB}} + \nabla \cdot Q^{\mathrm{MB}} = Z, \tag{73}$$

where we have introduced a short-hand notation for the total stress, including both the shear and the bulk contributions,

$$Z = P\left(\nabla u + \nabla u^\dagger - \frac{2}{3}(\nabla \cdot u)I\right) + P\left(\frac{2}{3} - \frac{R}{C_v}\right)(\nabla \cdot u)I, \tag{74}$$

and where $(\cdot)^\dagger$ denotes transposition. With (73) and (74), the non-equilibrium pressure tensor (70) becomes,

$$P^{(1)} = -\frac{1}{\omega} Z - \frac{1}{\omega} \nabla \cdot \tilde{Q} + P^{\mathrm{ex}(1)}. \tag{75}$$

A comment is in order. In (75), the first term is the conventional contribution from both the shear and the bulk stress. The second term is anomalous due to the diagonal anisotropy (27) while the third is the counterterm required to annihilate the spurious contribution in the next, second-order approximation. According to (31),

$$\boldsymbol{P}^{\text{ex}(1)} = \left(\frac{2-\omega}{2\omega}\right)\boldsymbol{\nabla}\cdot\tilde{\boldsymbol{Q}}. \tag{76}$$

Similarly, the first-order constitutive relation for the nonequilibrium energy flux $\boldsymbol{q}^{(1)}$ is found from (61),

$$-\omega_1\boldsymbol{q}^{(1)} - (\omega-\omega_1)\boldsymbol{q}^{*(1)} = \partial_t^{(1)}\boldsymbol{q}^{\text{eq}} + \boldsymbol{\nabla}\cdot\boldsymbol{R}^{\text{eq}}. \tag{77}$$

Evaluating the right-hand side of (77) with the help of the first-order relations (66), (67), and (69), we obtain

$$\partial_t^{(1)}\boldsymbol{q}^{\text{eq}} + \boldsymbol{\nabla}\cdot\boldsymbol{R}^{\text{eq}} = PC_p\boldsymbol{\nabla}T + (\boldsymbol{u}\cdot\boldsymbol{Z}). \tag{78}$$

With (78), the nonequilibrium energy flux (77) becomes

$$\boldsymbol{q}^{(1)} = -\frac{1}{\omega_1}PC_p\boldsymbol{\nabla}T - \frac{1}{\omega_1}(\boldsymbol{u}\cdot\boldsymbol{Z}) - \frac{\omega-\omega_1}{\omega_1}\boldsymbol{q}^{*(1)}. \tag{79}$$

The quasi-equilibrium energy flux $\boldsymbol{q}^{*(1)}$ is evaluated according to (46) and by taking into account the first-order constitutive relation for the pressure tensor (75),

$$\boldsymbol{q}^{*(1)} = \boldsymbol{u}\cdot\left(\boldsymbol{P}^{(1)} + \frac{1}{2}\boldsymbol{\nabla}\cdot\tilde{\boldsymbol{Q}}\right) = -\frac{1}{\omega}(\boldsymbol{u}\cdot\boldsymbol{Z}). \tag{80}$$

We comment that the first term in the nonequilibrium energy flux (79) is a precursor of the Fourier law of thermal conductivity while the second and the third terms combine to the viscous heating contribution, as we shall see it below. The quasi-equilibrium flux (80) is required for consistency of the viscous heating with the prescribed Prandtl number.[31]

With the first-order constitutive relations for the nonequilibrium fluxes (75) and (79) in place, we proceed to the second-order approximation. Applying the solvability condition (63) and (64) to the second-order f-equation (59), we obtain

$$\partial_t^{(2)}\rho = 0, \tag{81}$$

$$\partial_t^{(2)}(\rho\boldsymbol{u}) = -\boldsymbol{\nabla}\cdot\left[\left(1-\frac{\omega}{2}\right)\boldsymbol{P}^{(1)} + \frac{\omega}{2}\boldsymbol{P}^{\text{ex}(1)}\right]. \tag{82}$$

The second-order momentum equation (82) is transformed by virtue of (75) and (76) to give

$$\partial_t^{(2)}(\rho\boldsymbol{u}) = -\boldsymbol{\nabla}\cdot\left[-\left(\frac{1}{\omega}-\frac{1}{2}\right)\boldsymbol{Z}\right]. \tag{83}$$

Note that, the anomalous terms cancel out and the result (83) is manifestly isotropic.

Finally, applying solvability condition (65) to the second-order g-equation (62), we find

$$\partial_t^{(2)}(\rho E) = -\boldsymbol{\nabla}\cdot\left[\left(1-\frac{\omega_1}{2}\right)\boldsymbol{q}^{(1)} - \frac{\omega-\omega_1}{2}\boldsymbol{q}^{*(1)}\right]. \tag{84}$$

Taking into account the first-order energy flux (79) and the quasi-equilibrium energy flux (80), we obtain in (84),

$$\partial_t^{(2)}(\rho E) = -\boldsymbol{\nabla}\cdot\left[-\left(\frac{1}{\omega_1}-\frac{1}{2}\right)C_p P\boldsymbol{\nabla}T\right] - \boldsymbol{\nabla}\cdot\left[-\left(\frac{1}{\omega}-\frac{1}{2}\right)(\boldsymbol{u}\cdot\boldsymbol{Z})\right]. \tag{85}$$

While the first term leads to the Fourier law, it is important to note that the second term represents viscous heating consistent with the

momentum equation (83). The latter consistency is implied by the construction of the quasi-equilibrium energy flux (46) and (80). This concludes the second-order accurate analysis of the hydrodynamic limit of the LBM system (1) and (2), and we proceed with a summary of the gas dynamics equations thereby recovered.

F. Equations of gas dynamics

Combining the first- and second-order contributions to the density, the momentum,, and the energy equation, (66) and (81), (67) and (83), and (68) and (85), respectively, and using a notation, $\partial_t = \partial_t^{(1)} + \delta t \partial_t^{(2)}$, we arrive at the continuity, the flow and the energy equations of gas dynamics as follows:

$$\partial_t\rho + \boldsymbol{\nabla}\cdot(\rho\boldsymbol{u}) = 0, \tag{86}$$

$$\partial_t(\rho\boldsymbol{u}) + \boldsymbol{\nabla}\cdot(\rho\boldsymbol{u}\otimes\boldsymbol{u}) + \boldsymbol{\nabla}\cdot\boldsymbol{\pi} = 0, \tag{87}$$

$$\partial_t(\rho E) + \boldsymbol{\nabla}\cdot(\rho E\boldsymbol{u}) + \boldsymbol{\nabla}\cdot\boldsymbol{q} + \boldsymbol{\nabla}\cdot(\boldsymbol{\pi}\cdot\boldsymbol{u}) = 0. \tag{88}$$

Here, $\boldsymbol{\pi}$ is the pressure tensor

$$\boldsymbol{\pi} = P\boldsymbol{I} - \mu\left(\boldsymbol{S} - \frac{2}{3}(\boldsymbol{\nabla}\cdot\boldsymbol{u})\boldsymbol{I}\right) - \varsigma(\boldsymbol{\nabla}\cdot\boldsymbol{u})\boldsymbol{I}, \tag{89}$$

with P the pressure of ideal gas,

$$P = \rho RT, \tag{90}$$

with the strain rate tensor

$$\boldsymbol{S} = \boldsymbol{\nabla}\boldsymbol{u} + \boldsymbol{\nabla}\boldsymbol{u}^{\dagger}, \tag{91}$$

and the dynamic viscosity μ and the bulk viscosity ς,

$$\mu = \left(\frac{1}{\omega}-\frac{1}{2}\right)P\delta t, \tag{92}$$

$$\varsigma = \left(\frac{2}{3}-\frac{R}{C_v}\right)\mu. \tag{93}$$

The heat flux $\boldsymbol{q}$ in the energy equation (88) reads

$$\boldsymbol{q} = -\kappa\boldsymbol{\nabla}T, \tag{94}$$

with the thermal conductivity coefficient κ,

$$\kappa = \left(\frac{1}{\omega_1}-\frac{1}{2}\right)C_p P\delta t. \tag{95}$$

The Prandtl number due to (92) and (95) is

$$\text{Pr} = \frac{C_p\mu}{\kappa} = \frac{\omega_1(2-\omega)}{\omega(2-\omega_1)}, \tag{96}$$

while the adiabatic exponent,

$$\gamma = \frac{C_p}{C_v}, \tag{97}$$

is defined by the choice of the caloric equations of state (6) and Mayer's relation, $C_p - C_v = R$. The mass, momentum, and energy equations, (86), (87), and (88) are the standard equations of the macroscopic gas dynamics. We shall conclude the model development with a summary of the key elements of the LBM system (1) and (2).

G. Summary of the lattice Boltzmann model

The two-population lattice Boltzmann model (1) and (2) on the standard $D3Q27$ discrete velocity set introduced by Karlin *et al.*[31] is extended to the compressible flow simulation following the three key modifications:

- The product-form extended equilibrium for the momentum lattice, Eqs. (12), (30), and (28):

$$f_i^{\text{ex}} = \rho \Psi_{c_{ix}}(u_x, \mathcal{P}_{xx}^{\text{ex}}) \Psi_{c_{iy}}(u_y, \mathcal{P}_{yy}^{\text{ex}}) \Psi_{c_{iz}}(u_z, \mathcal{P}_{zz}^{\text{ex}});$$

- the operator product-form equilibrium for the energy lattice, Eqs. (7), (33), (12), and (42):

$$g_i^{\text{eq}} = \rho \Psi_{c_{ix}}(\mathcal{O}_x, \mathcal{O}_x^2) \Psi_{c_{iy}}(\mathcal{O}_y, \mathcal{O}_y^2) \Psi_{c_{iz}}(\mathcal{O}_z, \mathcal{O}_z^2) E;$$

- the quasi-equilibrium for the energy lattice is made consistent with both of the above, Eqs. (44) and (46):

$$g_i^* = \begin{cases} g_i^{\text{eq}} + \dfrac{1}{2} \boldsymbol{c}_i \cdot (\boldsymbol{q}^* - \boldsymbol{q}^{\text{eq}}) & \text{if } c_i^2 = 1 \\ g_i^{\text{eq}} & \text{otherwise.} \end{cases}$$

We shall proceed with the implementation of the compressible lattice Boltzmann model and numerical validation.

III. NUMERICAL RESULTS

A. General implementation issues

The spatial discretization of the deviation $\tilde{\boldsymbol{Q}}$ in Eqs. (31) and (46) has an important effect on the stability of the model, especially in the case of supersonic flows where discontinuities emerge in the flow field. It has been shown through linear stability analysis[22] that, while the second-order central difference scheme provides good stability domain in the subsonic regime, the first-order upwind scheme is necessary for maintaining the stability in the supersonic regime and capturing shock wave. We, therefore, employ the first-order upwind scheme in order to have a wider stability domain.

For example, the x-derivative of the deviation $\tilde{Q}_{xxx}$ at grid point $\boldsymbol{x}_{i,j,k}$ can be written as

$$\partial_x \tilde{Q}_{xxx,(i,j,k)} = \frac{\tilde{Q}_{xxx,(i+1/2,j,k)} - \tilde{Q}_{xxx,(i-1/2,j,k)}}{\Delta x}, \tag{98}$$

where (omitting xxx and j, k indices) $\tilde{Q}_{i+1/2}$ and $\tilde{Q}_{i-1/2}$ are upwind reconstruction of $\tilde{Q}$ at the interface $\boldsymbol{x}_{i\pm1/2,j,k}$,

$$\tilde{Q}_{i+1/2} = \begin{cases} \tilde{Q}_i & \text{if } u_x > 0 \\ \tilde{Q}_{i+1} & \text{otherwise.} \end{cases} \tag{99}$$

The performance and accuracy of the proposed LBM for compressible flow is tested numerically through the simulation of benchmark cases. First, the Sod shock tube problem is considered. Second, we show the ability of the model in capturing moderately supersonic shock waves, through simulation of shock–vortex interaction. Finally, the model is tested with a compressible turbulence problem, i.e., decaying of compressible homogeneous isotropic turbulence at different turbulent Mach numbers. All simulations are performed assuming constant specific heats with gas constant $R = 1$, adiabatic exponent $\gamma = 1.4$ and the $D3Q27$ lattice.

B. Sod's shock tube

Sod's shock tube benchmark[38] is a classical Riemann problem, which is often used to test capability of a compressible flow solver in capturing shock waves, contact discontinuities and expansion fans. The initial flow field is given by

$$(\rho, u_x, P) = \begin{cases} (1.0,\ 0,\ 0.15), & x/L_x \leq 0.5 \\ (0.125,\ 0,\ 0.015), & x/L_x > 0.5, \end{cases}$$

where $L_x = 600$ is the number of grid points. Simulation results with the viscosity $\mu = 0.015$ for the density and reduced velocity $u^* = u/\sqrt{T_l}$, where T_l is the temperature on the left half of tube, at the nondimensional time $t^* = t\sqrt{T_l}/L_x = 0.2$, are shown in Figs. 1 and 2. It can be seen that, apart from a small oscillation, the results match the nonviscous exact solution well.

C. Shock–vortex interaction

Sound generation by a vortex passing through a shock wave[39] is studied to assess the performance and accuracy of the developed model for supersonic flows involving shock. This problem consists of an isentropic vortex, with vortex Mach number Ma_v, initially in the upstream shock region, which is passed through a stationary shock wave at advection Mach number $\text{Ma}_a = 1.2$ with the left state $(\rho, T, u_x, u_y)_l = (1, 0.05, \text{Ma}_a\sqrt{\gamma T_l}, 0)$ and Rankine-Hugoniot right state. The initial field with standing shock $(\rho_\infty, P_\infty, u_{x,\infty}, u_{y,\infty})$ is perturbed with an isentropic vortex with radius r_v centered at (x_v, y_v),[39]

$$\rho = \rho_\infty \left[1 - \frac{\gamma - 1}{2} \text{Ma}_v^2 e^{(1-r^2)}\right]^{1/(\gamma-1)},$$

$$P = P_\infty \left[1 - \frac{\gamma - 1}{2} \text{Ma}_v^2 e^{(1-r^2)}\right]^{\gamma/(\gamma-1)},$$

$$u_x = u_{x,\infty} + \sqrt{\gamma T_l} \text{Ma}_v \frac{(y - y_v)}{r_v} e^{(1-r^2)/2},$$

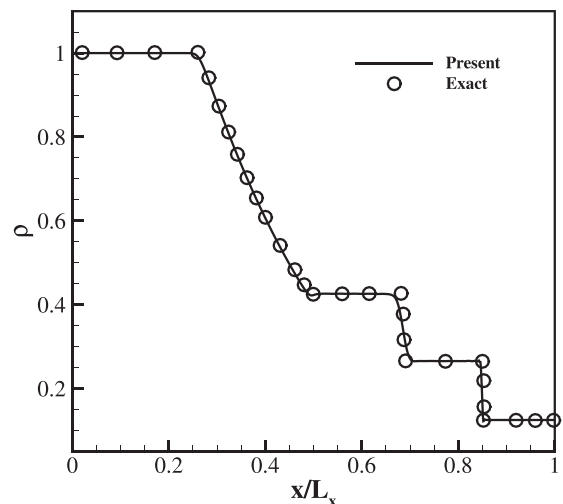$$u_y = u_{y,\infty} - \sqrt{\gamma T_l} \text{Ma}_v \frac{(x - x_v)}{r_v} e^{(1-r^2)/2},$$

FIG. 1. Density profile for Sod's shock tube simulation at nondimensional time $t^* = 0.2$. Line: present model; symbols: exact solution.
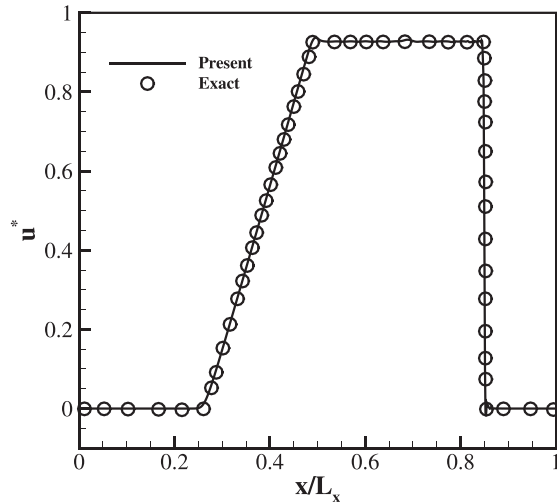
FIG. 2. Reduced velocity profile for Sod's shock tube simulation at nondimensional time $t^* = 0.2$. Line: present model; symbols: exact solution.

where $r = \sqrt{(x - x_v)^2 + (y - y_v)^2}/r_v$ is the reduced radius and the shock is initially located at $x_s = 8r_v$.

We perform a simulation with $\mathrm{Ma}_a = 1.2$, $\mathrm{Ma}_v = 0.25$, where the Reynolds number is set to be $\mathrm{Re} = \frac{\rho_l c_{s,l} r_v}{\mu} = 800$, $c_{s,l}$ is the speed of sound upstream of the shock, and the Prandtl number is $\mathrm{Pr} = 0.75$. The computational domain size is $L_x \times L_y = 1680 \times 1440$, the vortex radius is $r_v = L_x/28$ and the vortex center is at $(x_v, y_v) = (6r_v, L_y/2)$.

Figure 3 shows the sound pressure contours at time $t^* = 6$, where the sound pressure is defined as, $\Delta P = (P - P_s)/P_s$, and P_s is the pressure behind the shock wave. The shock wave deformation caused by the interaction with the vortex is observed. To quantify the accuracy of the computations, the radial sound pressure distribution is plotted in Fig. 4 in comparison with the direct numerical simulation (DNS) results.[39] The sound pressure is measured in the radial direction with the origin at the vortex center, at an angle $\theta = -45°$ and at three different nondimensional times $t^* = 6, 8, 10$, where
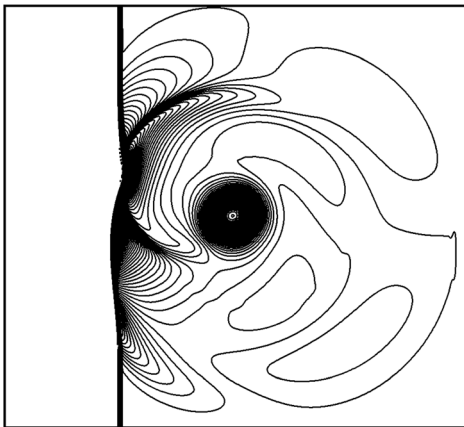
FIG. 3. The sound pressure field ΔP for the shock–vortex interaction with $\mathrm{Ma}_a = 1.2$, $\mathrm{Ma}_v = 0.25$, and $\mathrm{Re} = 800$ at $t^* = 6$. The contour levels are from $\Delta P_{min} = -0.48$ to $\Delta P_{max} = 0.16$ with an increment of $0.003\,216$.
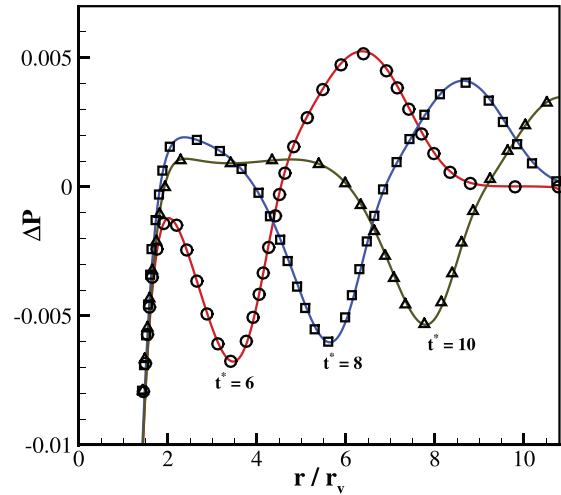

FIG. 4. Comparison of radial sound pressure distribution ΔP for $\mathrm{Ma}_a = 1.2$, $\mathrm{Ma}_v = 0.25$, and $\mathrm{Re} = 800$ with the DNS results at three different times $t^* = 6, 8, 10$. Lines: present model; symbol: DNS.[39]

$t^* = tc_{s,l}/r_v$. Excellent agreement is observed between the present model and the DNS.[39] Note that the sound pressure is typically a small perturbation (around 1%) on top of the hydrodynamic pressure. This shows that the present model with the LBGK collision term can accurately capture moderately supersonic shock waves.

D. Decaying of compressible isotropic turbulence

To demonstrate that the present compressible model is a reliable method for the simulation of complex flows involving both turbulence and shocks, decaying compressible homogeneous isotropic turbulence in a periodic box is considered as the final test-case. This problem has been studied extensively[40–47] and is a challenging test-case, as it contains both compressibility effects and shocks, as well as turbulent structures in the flow field.[43]

The initial condition in a cubic domain with the side L is set to be unit density and constant temperature along with a divergence-free velocity field which follows the specified energy spectrum,

$$E(\kappa) = A\kappa^4 \exp\left(-2(\kappa/\kappa_0)^2\right), \tag{100}$$

where κ is the wave number, κ_0 is the wave number at which the spectrum peaks and the amplitude A controls the initial kinetic energy.[42] The method of kinematic simulation[48] is used to generate the velocity field.

Control parameters for this problem are the turbulent Mach number,

$$\mathrm{Ma}_t = \frac{\sqrt{\langle \boldsymbol{u} \cdot \boldsymbol{u} \rangle}}{\langle c_s \rangle}, \tag{101}$$

and the Reynolds number based on the Taylor microscale,

$$\mathrm{Re}_\lambda = \frac{\langle \rho \rangle u_{rms} \lambda}{\mu_0}, \tag{102}$$

where $u_{rms} = \sqrt{\langle \boldsymbol{u} \cdot \boldsymbol{u} \rangle/3}$ is the root mean square (rms) of the velocity and notation $\langle \cdots \rangle$ stands for the volume averaging over the entire computational domain while λ is the Taylor microscale,

$$\lambda^2 = \frac{\langle u_x^2 \rangle}{\langle (\partial_x u_x)^2 \rangle}. \tag{103}$$

The dynamic viscosity is following a power-law dependence on temperature,

$$\mu = \mu_0 \left(\frac{T}{T_0} \right)^{0.76}, \tag{104}$$

with T_0 being the initial temperature. The Prandtl number for all the simulations is $Pr = 0.7$ in accordance with the DNS.[42]

1. Low turbulent Mach number

The simulation is first performed at a relatively low turbulent Mach number $Ma_t = 0.3$ with $Re_\lambda = 72$, $\kappa_0 = 8(2\pi/L)$ and initial temperature $T_0 = 0.15$. Figure 5 illustrates the instantaneous iso-surface of the velocity divergence $\mathbf{\nabla} \cdot \mathbf{u}$ colored with the local Mach number at the nondimensional time $t^* = t/\tau = 0.4$, where $\tau = L_I/u_{rms,0}$ is the large eddy turnover time defined based on the initial rms of the velocity and the integral length scale,

$$L_I = \frac{3\pi \int_0^\infty [E(\kappa)/\kappa]d\kappa}{4 \int_0^\infty E(\kappa)d\kappa} = \frac{\sqrt{2\pi}}{\kappa_0}. \tag{105}$$

It is observed that in this case, the flow is in a moderately compressible to a high-subsonic regime, with the maximum local Mach number $Ma_{max} \sim 0.8$.

In order to quantify the validity of the model, a grid convergence study is performed by using three domain sizes, 64^3, 128^3, and 256^3. The decay of the turbulent Mach number and of the turbulent kinetic

FIG. 6. Decay of the turbulent Mach number for compressible decaying turbulence at $Ma_t = 0.3$ and $Re_\lambda = 72$. Lines: present model; symbol: DNS.[42]

energy $K = 1/2\langle \rho u^2 \rangle$ are shown in Figs. 6 and 7, where the convergence to the DNS results[42] can be observed.

To assess the effect of compressibility, time evolution of the rms of dilatation,

$$\theta_{rms} = \sqrt{\langle (\mathbf{\nabla} \cdot \mathbf{u})^2 \rangle}, \tag{106}$$

is compared in Fig. 8 with the DNS, where dilatation is normalized with the initial rms of vorticity, $\omega_{rms,0} = \sqrt{\langle |\tilde{\omega}_0|^2 \rangle}$, and $\tilde{\omega} = \nabla \times \mathbf{u}$. Strong compressibility effects can be seen at the initial stage, where dilatation rapidly increases from its initial value $\theta_{rms,0} = 0$, followed by a monotonic decay. Furthermore, the rms of the density $\rho_{rms} = \sqrt{\langle \rho^2 \rangle - \langle \rho \rangle^2}$ normalized by $Ma_{t,0}^2$ is shown in Fig. 9. Also here the agreement with the DNS is quite satisfactory with 256^3 grid points.

FIG. 5. Iso-surface of velocity divergence $\mathbf{\nabla} \cdot \mathbf{u} = 0.005$, colored by local Mach number for compressible decaying turbulence at $Ma_t = 0.3$, $Re_\lambda = 72$, and $t^* = 0.4$.
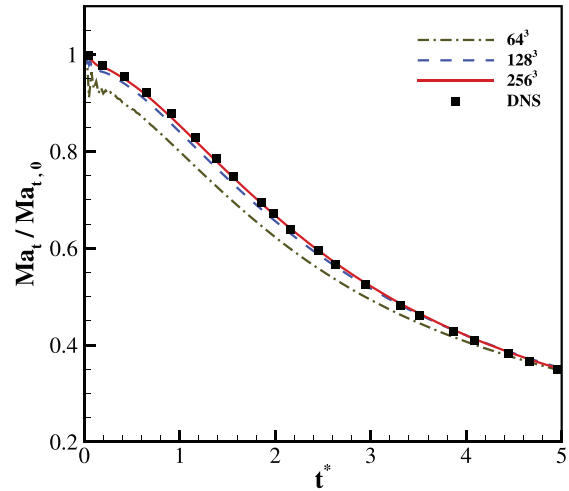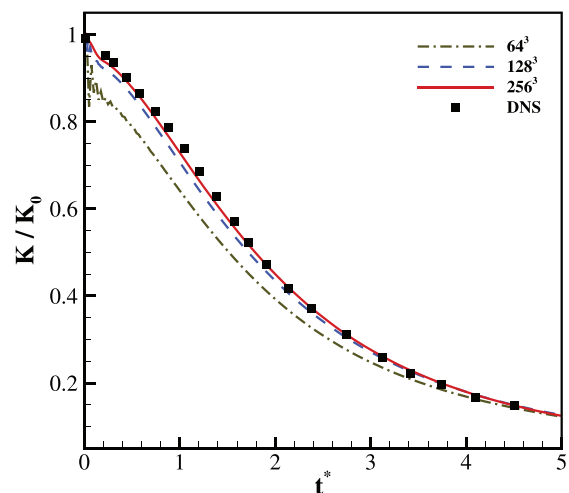
FIG. 7. Decay of the turbulent kinetic energy for compressible decaying turbulence at $Ma_t = 0.3$ and $Re_\lambda = 72$. Lines: present model; symbol: DNS.[42]
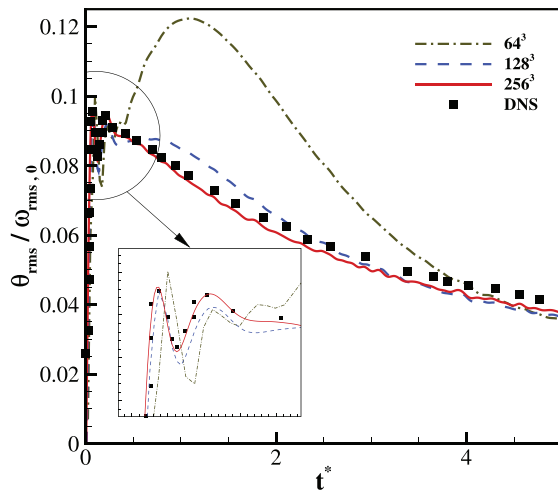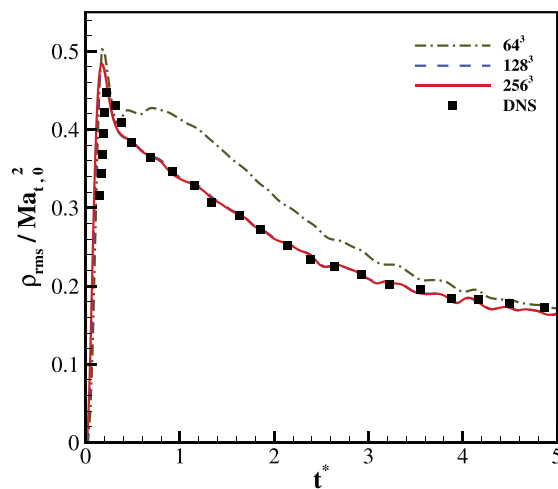
FIG. 8. Time history of root mean square of dilitation for compressible decaying turbulence at $Ma_t = 0.3$ and $Re_\lambda = 72$. Lines: present model; symbol: DNS.[42]
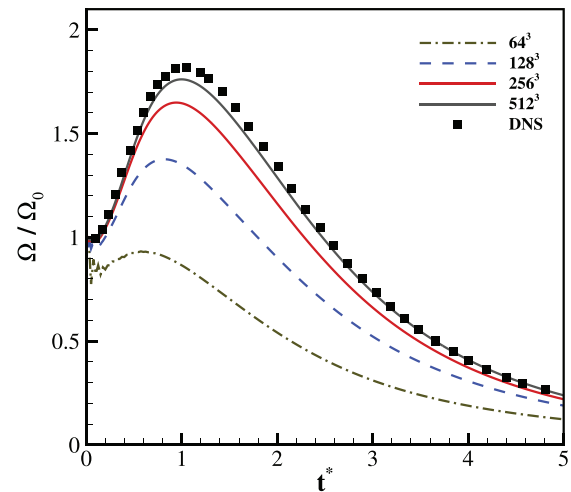

FIG. 10. Time history of enstrophy for compressible decaying turbulence at $Ma_t = 0.3$ and $Re_\lambda = 72$. Lines: present model; symbol: DNS.[49]

The enstrophy defined as

$$\Omega = \frac{1}{2} \langle \widetilde{\omega}^2 \rangle \qquad (107)$$

is a sensitive variable to analyze the performance of a numerical scheme for turbulent flows, as it is closely related to small-scale turbulence motions.[49,50] The temporal evolution of the enstrophy normalized with its initial value is compared in Fig. 10 with the DNS results of the spectral method reported in Fang *et al.*[49] It can be seen that in all cases the enstrophy increases in the beginning due to vortex stretching, which generates small-scale turbulence structures. This makes the viscous dissipation stronger, which leads to a decrease in enstrophy.[50] Furthermore, coarse simulations result in under-prediction of peak value and also fast decay rate, due to strong suppression of small-scale

fluctuations. Here, contrary to the previous cases, 256^3 grid size is not enough to accurately capture the statistics. By increasing the resolution to 512^3, the peak value and decay rate of enstrophy can be captured with good accuracy. This further confirms the accuracy of the present model in capturing the physics of compressible turbulence. Moreover, the convergence order of the model is evaluated based on the L_∞ error of enstrophy with respect to the DNS results. As shown in Fig. 11, the overall accuracy in space is slightly below second-order.

2. Effect of deviation discretization on the accuracy

As pointed out earlier, first-order upwind discretization of the deviation term is necessary for preventing the Gibbs phenomenon and maintaining the stability of the model in supersonic regime.
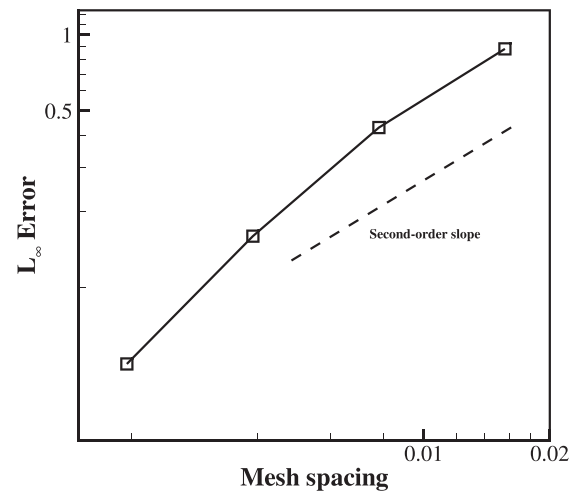

FIG. 9. Time history of root mean square of density for compressible decaying turbulence at $Ma_t = 0.3$ and $Re_\lambda = 72$. Lines: present model; symbol: DNS.[42]

FIG. 11. Convergence rate of enstrophy for grid resolutions 64^3 to 512^3. Symbols: L_∞ error of enstrophy with respect to the DNS results; dashed line: second-order slope.
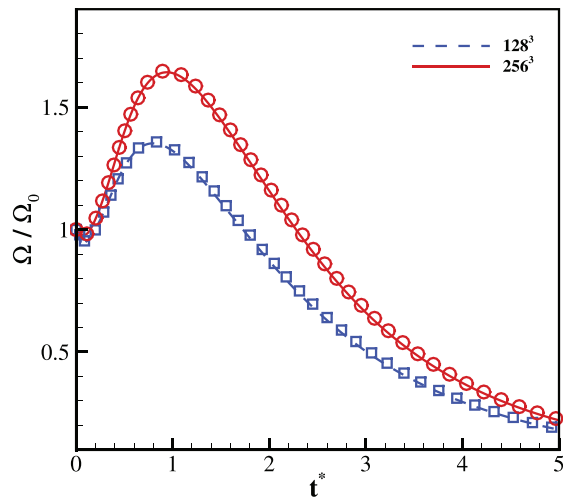
FIG. 12. Effect of deviation discretization on the enstrophy evolution for compressible decaying turbulence at $Ma_t = 0.3$ and $Re_\lambda = 72$. Lines: present model with first-order upwind discretization of deviation term; symbols: present model with second-order central difference discretization of deviation term.

FIG. 14. Decay of the turbulent kinetic energy for compressible decaying turbulence at $Ma_t = 0.5$ and $Re_\lambda = 72$. Lines: present model; symbol: DNS.[42]

Here, we investigate the effect of the discretization scheme on the accuracy in subsonic turbulent regime, by comparing the results to the case with the second-order central evaluation of derivatives of deviation term. It can be seen from Fig. 12 that, the time history of enstrophy is insensitive to the evaluation of deviation term. All other turbulence statistics showed similar behavior, but are not presented here for the sake of brevity. This indicates that the use of a first-order scheme does not degrade the formal accuracy of the solver (shown in Fig. 11), although it provides sufficient dissipation for stabilizing the solver and capturing the shock.
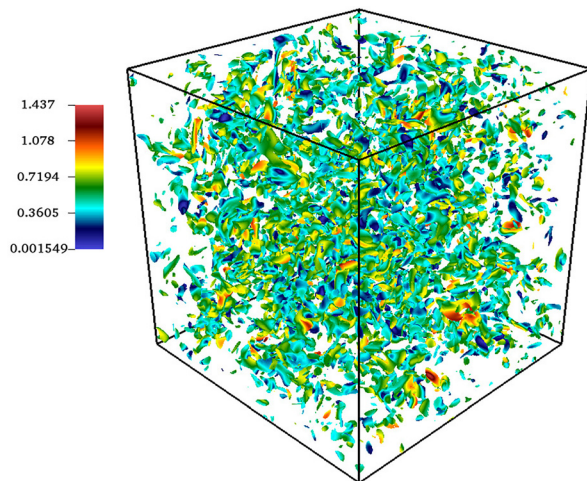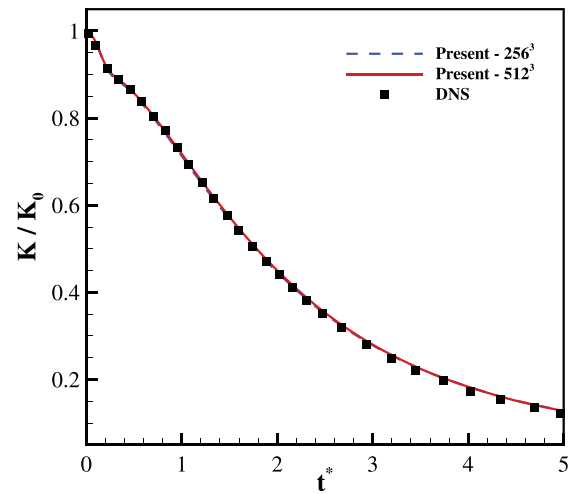
3. High turbulent Mach number

We now move on to a higher turbulent Mach number. It is well known that at sufficient high turbulent Mach numbers, random shock waves commonly known as eddy-shocklets appear in the flow,[40,42,43] due to compressibility and turbulent motions. This scenario can, therefore, be considered as a rigorous test case for the validity of the present model.

We increase the turbulent Mach number to $Ma_t = 0.5$ and perform the simulation with 256^3 and 512^3 grid points and the same Reynolds number $Re_\lambda = 72$. The iso-surface of the velocity divergence colored by local Mach number is shown in Fig. 13, which confirms the presence of local supersonic regions during the decay. Moreover, to show that the model can accurately predict turbulent statistics in the presence of shocks, time evolution of the turbulent kinetic energy, rms

FIG. 13. Iso-surface of velocity divergence $\nabla \cdot \boldsymbol{u} = 0.015$, colored by local Mach number for compressible decaying turbulence at $Ma_t = 0.5$, $Re_\lambda = 72$, and $t^* = 0.4$.
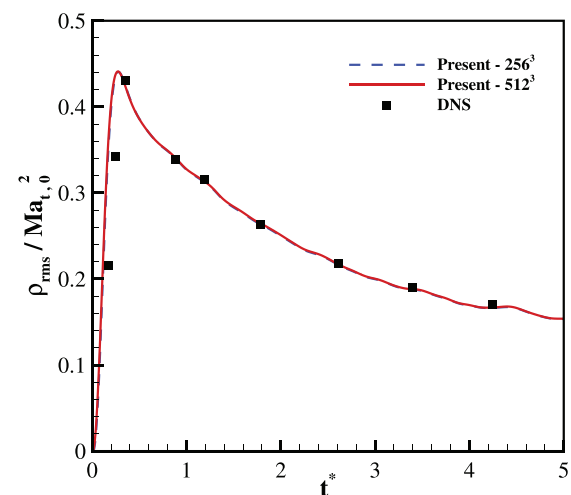

FIG. 15. Time history of root mean square of density for compressible decaying turbulence at $Ma_t = 0.5$ and $Re_\lambda = 72$. Lines: present model; symbol: DNS.[42]
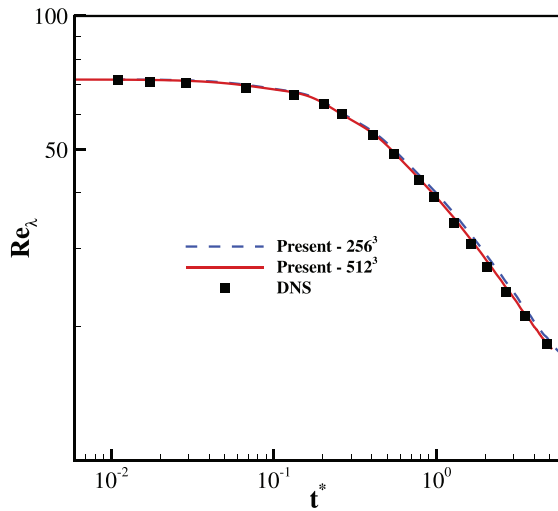
FIG. 16. Time history of Taylor microscale Reynolds number for compressible decaying turbulence at $Ma_t = 0.5$ and $Re_\lambda = 72$. Lines: present model; symbol: DNS.[42]

FIG. 18. Time history of the dissipation rate for compressible decaying turbulence at $Ma_t = 0.488$ and $Re_\lambda = 175$. Line: present model; symbol: DNS.[42]

of density and Taylor microscale Reynolds number are plotted in Figs. 14–16, respectively. Here also the results agree well with the reference DNS results.

As a final validation case, we investigate the performance of the model at a relatively high Reynolds number of $Re_\lambda = 175$, while keeping the turbulent Mach number high enough $Ma_t = 0.488$. The initial spectrum peaks at $\kappa_0 = 4(2\pi/L)$ in this case.

History of turbulent kinetic energy, solenoidal dissipation rate $\epsilon = \langle \mu\omega^2 \rangle$ and Taylor miroscale Reynolds number (102) are plotted in Figs. 17–19, using 768^3 grid points. The results agree well with the reference DNS solution.[42] The energy spectrum at various times is shown in Fig. 20. It is observed that initially, large scales contain most

of the energy and as time evolves the energy is transferred to small scales. Moreover, since the Reynolds number is high enough, the spectrum shows the inertial range with slope of $\kappa^{-5/3}$ which further confirms the accuracy of the results and shows the ability of the model in capturing broadband turbulent motions in the presence of shocks.

IV. CONCLUSION

In this work, we proposed a lattice Boltzmann framework for the simulation of compressible flows on standard lattices. The product-form factorization was used to represent all pertinent equilibrium and quasi-equilibrium populations. The well-known anomaly of the standard lattices was eliminated by redefining the diagonal components of
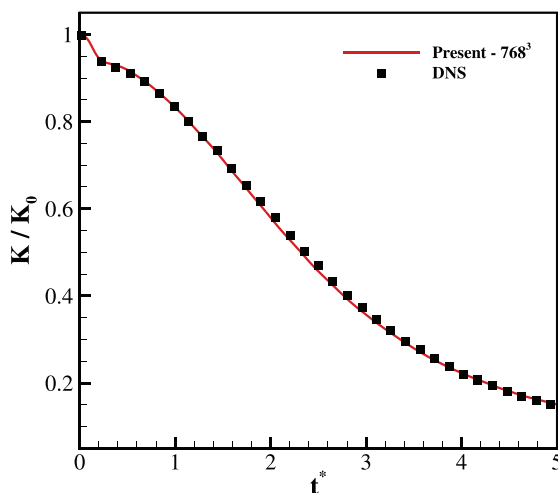

FIG. 17. Decay of the turbulent kinetic energy for compressible decaying turbulence at $Ma_t = 0.488$ and $Re_\lambda = 175$. Line: present model; symbol: DNS.[42]
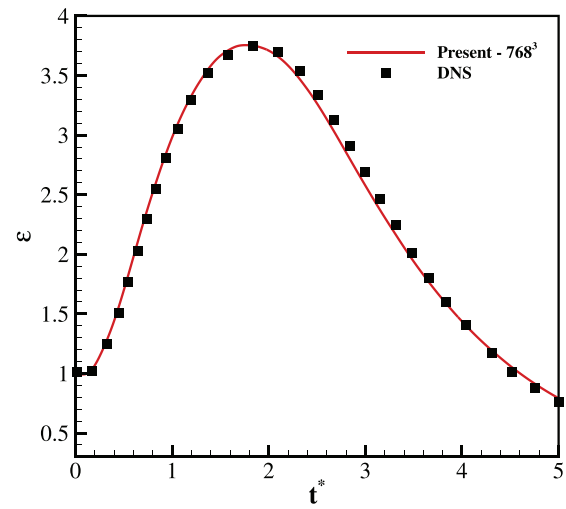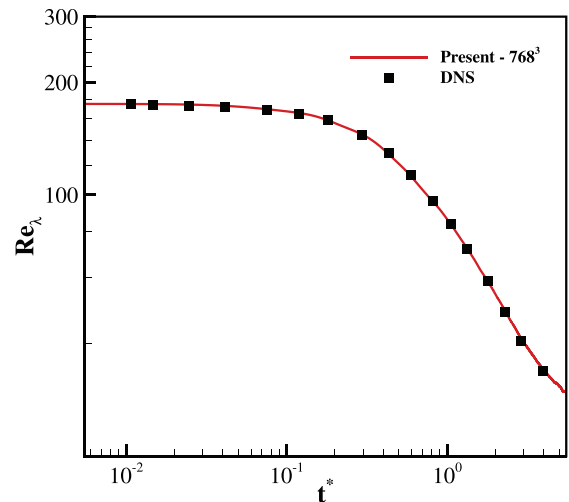

FIG. 19. Time history of Taylor microscale Reynolds number for compressible decaying turbulence at $Ma_t = 0.488$ and $Re_\lambda = 175$. Line: present model; symbol: DNS.[42]
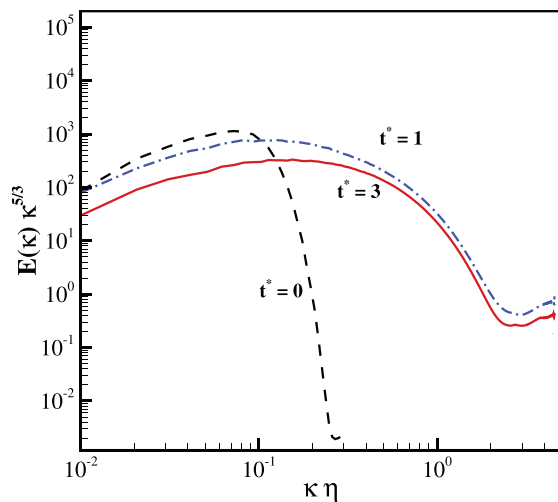
FIG. 20. Energy spectrum at various times ($t^* = 0, 1,$ and 3) for compressible decaying turbulence at $Ma_t = 0.488$ and $Re_\lambda = 175$. Dashed line is the initial spectrum ($t^* = 0$). Here, η is the Kolmogorov length scale.

the equilibrium pressure tensor through adding an appropriate correction term. The analysis of the model was conducted through simulation of the Sod's shock tube, sound generation in shock–vortex interaction and compressible decaying homogeneous isotropic turbulence.

It was demonstrated that the present fully on-lattice model with the single relaxation time LBGK collision term is able to properly predict the relevant features of the compressible flows. In particular, the model can capture moderately supersonic shock waves up to Ma ~ 1.5. Furthermore, the simulation of compressible decaying turbulence demonstrated that the model can accurately capture compressibility effects, turbulence fluctuations and shocks. It was shown that the model performs well even at high turbulent Mach number, where eddy-shocklets exist in the flow field and interact with turbulence. The results of the model were found to be in good agreement with DNS results.

Overall, the promising results of the proposed model on standard lattices open interesting prospects toward the numerical simulation of more complex applications such as compressible jet flow,[51] shock turbulence[52,53] or shock boundary-layer interactions.[54,55] Moreover, the model could be augmented with more sophisticated collision terms in order to enhance the stability of under-resolved simulations. This will be the focus of our future research.

DATA AVAILABILITY

The data that support the findings of this study are available within the article.

REFERENCES

[1]D. A. Caughey, *Computational Aerodynamics* (Elsevier, 2003).

[2]J. von Neumann and R. D. Richtmyer, "A method for the numerical calculation of hydrodynamic shocks," J. Appl. Phys. **21**, 232–237 (1950).

[3]C.-W. Shu, "High order ENO and WENO schemes for computational fluid dynamics," in *High-Order Methods for Computational Physics* (Springer, 1999), pp. 439–582.

[4]A. Subramaniam, M. L. Wong, and S. K. Lele, "A high-order weighted compact high resolution scheme with boundary closures for compressible turbulent flows with shocks," J. Comput. Phys. **397**, 108822 (2019).

[5]L. Fu, X. Y. Hu, and N. A. Adams, "A new class of adaptive high-order targeted ENO schemes for hyperbolic conservation laws," J. Comput. Phys. **374**, 724–751 (2018).

[6]L. Fu, "A very-high-order TENO scheme for all-speed gas dynamics and turbulence," Comput. Phys. Commun. **244**, 117–131 (2019).

[7]T. Haga and S. Kawai, "On a robust and accurate localized artificial diffusivity scheme for the high-order flux-reconstruction method," J. Comput. Phys. **376**, 534–563 (2019).

[8]M. Visbal and D. Gaitonde, "Shock capturing using compact-differencing-based methods," in 43rd AIAA Aerospace Sciences Meeting and Exhibit (2005), p. 1265.

[9]B. Dorschner, F. Bösch, S. S. Chikatamarla, K. Boulouchos, and I. V. Karlin, "Entropic multi-relaxation time lattice Boltzmann model for complex flows," J. Fluid Mech. **801**, 623 (2016).

[10]A. Wagner, "Thermodynamic consistency of liquid-gas lattice Boltzmann simulations," Phys. Rev. E **74**, 056703 (2006).

[11]M. Mendoza, B. Boghosian, H. J. Herrmann, and S. Succi, "Fast lattice Boltzmann solver for relativistic hydrodynamics," Phys. Rev. Lett. **105**, 014502 (2010).

[12]X. Shan, X.-F. Yuan, and H. Chen, "Kinetic theory representation of hydrodynamics: A way beyond the Navier–Stokes equation," J. Fluid Mech. **550**, 413–441 (2006).

[13]S. S. Chikatamarla and I. V. Karlin, "Lattices for the lattice Boltzmann method," Phys. Rev. E **79**, 046701 (2009).

[14]N. Frapolli, S. S. Chikatamarla, and I. V. Karlin, "Entropic lattice Boltzmann model for gas dynamics: Theory, boundary conditions, and implementation," Phys. Rev. E **93**, 063302 (2016).

[15]D. Wilde, A. Krämer, D. Reith, and H. Foysi, "Semi-Lagrangian lattice Boltzmann method for compressible flows," Phys. Rev. E **101**, 053306 (2020).

[16]N. Frapolli, "Entropic lattice Boltzmann models for thermal and compressible flows," Ph.D. thesis (ETH Zurich, 2017).

[17]N. I. Prasianakis and I. V. Karlin, "Lattice Boltzmann method for simulation of compressible flows on standard lattices," Phys. Rev. E **78**, 016704 (2008).

[18]N. I. Prasianakis, I. V. Karlin, J. Mantzaras, and K. B. Boulouchos, "Lattice Boltzmann method with restored Galilean invariance," Phys. Rev. E **79**, 066702 (2009).

[19]Z. Guo, C. Zheng, B. Shi, and T. Zhao, "Thermal lattice Boltzmann equation for low Mach number flows: Decoupling model," Phys. Rev. E **75**, 036704 (2007).

[20]Y. Feng, P. Sagaut, and W. Tao, "A three dimensional lattice model for thermal compressible flow on standard lattices," J. Comput. Phys. **303**, 514–529 (2015).

[21]M. H. Saadat, F. Bösch, and I. V. Karlin, "Lattice Boltzmann model for compressible flows on standard lattices: Variable Prandtl number and adiabatic exponent," Phys. Rev. E **99**, 013306 (2019).

[22]S. A. Hosseini, N. Darabiha, and D. Thévenin, "Compressibility in lattice Boltzmann on standard stencils: Effects of deviation from reference temperature," Philos. Trans. R. Soc. A **378**, 20190399 (2020).

[23]Y. Feng, P. Sagaut, and W.-Q. Tao, "A compressible lattice Boltzmann finite volume model for high subsonic and transonic flows on regular lattices," Comput. Fluids **131**, 45–55 (2016).

[24]Y. Feng, P. Sagaut, J. Jacob, and P. Sagaut, "Hybrid recursive regularized thermal lattice Boltzmann model for high subsonic compressible flows," J. Comput. Phys. **394**, 82–99 (2019).

[25]S. Guo, Y. Feng, and P. Sagaut, "Improved standard thermal lattice Boltzmann model with hybrid recursive regularization for compressible laminar and turbulent flows," Phys. Fluids **32**, 126108 (2020).

[26]F. Renard, Y. Feng, J.-F. Boussuge, and P. Sagaut, "Improved compressible hybrid lattice Boltzmann method on standard lattice for subsonic and supersonic flows," Comput. Fluids **219**, 104867 (2021).

[27]S. Zhao, G. Farag, P. Boivin, and P. Sagaut, "Toward fully conservative hybrid lattice Boltzmann methods for compressible flows," Phys. Fluids **32**, 126118 (2020).

[28]G. Farag, S. Zhao, T. Coratger, P. Boivin, G. Chiavassa, and P. Sagaut, "A pressure-based regularized lattice-Boltzmann method for the simulation of compressible flows," Phys. Fluids **32**, 066106 (2020).

[29]S. Guo, Y. Feng, and P. Sagaut, "On the use of conservative formulation of energy equation in hybrid compressible lattice Boltzmann method," Comput. Fluids **219**, 104866 (2021).

[30]Q. Li, K. Luo, Y. He, Y. Gao, and W. Tao, "Coupling lattice Boltzmann model for simulation of thermal flows on standard lattices," Phys. Rev. E **85**, 016710 (2012).

[31]I. Karlin, D. Sichau, and S. Chikatamarla, "Consistent two-population lattice Boltzmann model for thermal flows," Phys. Rev. E **88**, 063310 (2013).

[32]M. H. Saadat, F. Bösch, and I. V. Karlin, "Semi-Lagrangian lattice Boltzmann model for compressible flows on unstructured meshes," Phys. Rev. E **101**, 023311 (2020).

[33]N. Frapolli, S. S. Chikatamarla, and I. V. Karlin, "Lattice kinetic theory in a comoving Galilean reference frame," Phys. Rev. Lett. **117**, 010604 (2016).

[34]B. Dorschner, F. Bösch, and I. V. Karlin, "Particles on demand for kinetic theory," Phys. Rev. Lett. **121**, 130602 (2018).

[35]P. L. Bhatnagar, E. P. Gross, and M. Krook, "A model for collision processes in gases. I. Small amplitude processes in charged and neutral one-component systems," Phys. Rev. **94**, 511 (1954).

[36]I. Karlin and P. Asinari, "Factorization symmetry in the lattice Boltzmann method," Physica A **389**, 1530–1548 (2010).

[37]M. H. Saadat, B. Dorschner, and I. V. Karlin, "Extended lattice Boltzmann model," arXiv:2101.04550 (2021).

[38]G. A. Sod, "A survey of several finite difference methods for systems of nonlinear hyperbolic conservation laws," J. Comput. Phys. **27**, 1–31 (1978).

[39]O. Inoue and Y. Hattori, "Sound generation by shock-vortex interactions," J. Fluid Mech. **380**, 81–116 (1999).

[40]S. Lee, S. K. Lele, and P. Moin, "Eddy shocklets in decaying compressible turbulence," Phys. Fluids A **3**, 657–664 (1991).

[41]N. Mansour and A. Wray, "Decay of isotropic turbulence at low Reynolds number," Phys. Fluids **6**, 808–814 (1994).

[42]R. Samtaney, D. I. Pullin, and B. Kosović, "Direct numerical simulation of decaying compressible turbulence and shocklet statistics," Phys. Fluids **13**, 1415–1430 (2001).

[43]E. Johnsen, J. Larsson, A. V. Bhagatwala, W. H. Cabot, P. Moin, B. J. Olson, P. S. Rawat, S. K. Shankar, B. Sjögreen, H. C. Yee *et al.*, "Assessment of high-resolution methods for numerical simulations of compressible turbulence with shock waves," J. Comput. Phys. **229**, 1213–1237 (2010).

[44]G. Kumar, S. S. Girimaji, and J. Kerimo, "WENO-enhanced gas-kinetic scheme for direct simulations of compressible transition and turbulence," J. Comput. Phys. **234**, 499–523 (2013).

[45]K. Tanaka, T. Watanabe, K. Nagata, A. Sasoh, Y. Sakai, and T. Hayase, "Amplification and attenuation of shock wave strength caused by homogeneous isotropic turbulence," Phys. Fluids **30**, 035105 (2018).

[46]G. Cao, L. Pan, and K. Xu, "Three dimensional high-order gas-kinetic scheme for supersonic isotropic turbulence I: Criterion for direct numerical simulation," Comput. Fluids **192**, 104273 (2019).

[47]T. Chen, X. Wen, L.-P. Wang, Z. Guo, J. Wang, and S. Chen, "Simulation of three-dimensional compressible decaying isotropic turbulence using a redesigned discrete unified gas kinetic scheme," Phys. Fluids **32**, 125104 (2020).

[48]D. W. Meyer and M. L. Eggersdorfer, "Simulating particle collisions in homogeneous turbulence with kinematic simulation: A validation study," Colloids Surf. A **454**, 57–64 (2014).

[49]J. Fang, Y. Yao, Z. Li, and L. Lu, "Investigation of low-dissipation monotonicity-preserving scheme for direct numerical simulation of compressible turbulent flows," Comput. Fluids **104**, 55–72 (2014).

[50]E. Garnier, M. Mossi, P. Sagaut, P. Comte, and M. Deville, "On the use of shock-capturing schemes for large-eddy simulation," J. Comput. Phys. **153**, 273–311 (1999).

[51]V. Vuorinen, J. Yu, S. Tirunagari, O. Kaario, M. Larmi, C. Duwig, and B. Boersma, "Large-eddy simulation of highly underexpanded transient gas jets," Phys. Fluids **25**, 016101 (2013).

[52]J. Larsson and S. K. Lele, "Direct numerical simulation of canonical shock/turbulence interaction," Phys. Fluids **21**, 126101 (2009).

[53]S. Hickel, C. P. Egerer, and J. Larsson, "Subgrid-scale modeling for implicit large eddy simulation of compressible flows and shock-turbulence interaction," Phys. Fluids **26**, 106101 (2014).

[54]S. Pirozzoli, M. Bernardini, and F. Grasso, "Direct numerical simulation of transonic shock/boundary layer interaction under conditions of incipient separation," J. Fluid Mech. **657**, 361 (2010).

[55]L. Agostini, L. Larchevêque, and P. Dupont, "Mechanism of shock unsteadiness in separated shock/boundary-layer interactions," Phys. Fluids **27**, 126103 (2015).